

Model-based analysis of positive selection significantly expands the list of cancer driver genes, including RNA methyltransferases

Siming Zhao¹, Jun Liu², Pranav Nanga³, Yuwen Liu¹, A. Ercument Cicek⁴, Nicholas Knoblach¹, Chuan He², Matthew Stephens^{1,5,*}, and Xin He^{1,*}

¹*Department of Human Genetics, University of Chicago, Chicago, IL, 60637, USA*

²*Department of Chemistry, Department of Biochemistry and Molecular Biology, Institute for Biophysical Dynamics, Howard Hughes Medical Institute, University of Chicago, Chicago, IL, 60637, USA*

³*Department of Computer Science, University of Chicago, Chicago, IL, 60637, USA*

⁴*Computer Engineering Department, Bilkent University, Ankara 06800, Turkey, Computational Biology Department, Carnegie Mellon University, Pittsburgh, PA 15213 USA*

⁵*Department of Statistics, University of Chicago, Chicago, IL, 60637, USA*

*Correspondence should be addressed to M.S. (email: mstephens@uchicago.edu) or to X.H. (email: xinhe@uchicago.edu)

Abstract

Identifying driver genes is a central problem in cancer biology and has received great attentions from researchers. However, existing methods for detecting driver genes from somatic mutation data struggle to distinguish positive selection signals from highly heterogeneous background mutational processes. Here, we present a powerful statistical approach, driverMAPS (Model-based Analysis of Positive Selection) for driver gene identification. The key feature of driverMAPS is its modeling of mutation rates at the base-level, reflecting both background mutational processes and positive selection. Its selection model captures elevated mutation rates in functionally important sites using multiple external annotations, as well as spatial clustering of mutations. Its background mutation model accounts for both known covariates and local, gene-specific, variation caused by unknown factors. Applying driverMAPS to TCGA data across 20 tumor types identified 159 new potential driver genes. Cross-referencing this list with data from external sources strongly supports these findings. The novel genes include the mRNA methyltransferases METTL3-METTL14, and we experimentally validated the functional importance of somatic mutations in METTL3, confirming it as a potential tumor suppressor gene in bladder cancer.

Introduction

Cancer is caused by somatic mutations that confer a selective advantage to cells. Analyses of somatic mutation data from tumors can therefore help identify cancer-related (“driver”) genes, and this is a major motivation for recent large-scale cancer cohort sequencing projects¹. Indeed, such analyses have already identified hundreds of driver genes across many cancer types^{1,2}. Nonetheless, many important driver genes likely remain undiscovered³, especially in cancers with low sample sizes. Here we develop and apply new, more powerful, statistical methods to address this problem.

The basic idea underlying somatic mutation analyses is that genes exhibiting a high rate of somatic mutations are potential driver genes. However, mutation and repair processes are often significantly perturbed in cancer, so somatic mutations may also occur at a high rate in non-driver genes. Furthermore, somatic mutation rates vary substantially across genomic regions and across tumors. The challenge is to accurately distinguish driver genes against this complex background.

Several ideas have been developed to help address this challenge. One idea is to carefully model the background somatic mutation process. For example, the widely used method MutSigCV⁴ models this background by using features that correlate with somatic mutation rate, such as replication timing. Another idea is to model distinctive features of somatic mutations in driver genes. For example, driver genes may show an excess of nonsynonymous to synonymous mutations due to positive selection⁵, and mutations in driver genes tend to be more deleterious (“function bias”). Finally, somatic mutations in driver genes sometimes show a distinctive spatial pattern, tending to cluster together (e.g. in substrate binding sites). Methods that leverage one or more of these ideas include MuSiC⁶, MADGiC⁷, the OncoDrive suite^{8–10} and TUSON¹¹.

Here we refine and combine these key ideas to create a new integrated statistical framework for detecting cancer driver genes. Our model-based approach improves on existing methods in several ways. We improve the MutSigCV model for the background mutation process by accounting for local variation not captured by known genomic features. Our method also carefully models function bias at the base level, allowing the bias to depend on measures of functional importance such as conservation scores, SiFT¹² and PolyPhen¹³. And we use a Hidden Markov Model to capture potential spatial clustering of somatic mutations into “hotspots”. Finally, we exploit Bayesian hierarchical modelling to combine information across cancer types

and hence improve parameter estimates. We call our method driverMAPS (Model-based Analysis of Pattern of Selection).

We applied driverMAPS to TCGA exome sequencing data from 20 cancer types. The results suggest that driverMAPS is better able to detect previously known driver genes than existing methods, without excessive false positives. In addition, driverMAPS identified 159 new potential driver genes not identified by other methods. Both literature survey and extensive computational validation suggest that many of these genes are likely to be true driver genes. The novel potential driver genes included both METTL3 and METTL14, which together form a key enzyme for RNA methylation. We experimentally validated the functional relevance of somatic mutations in METTL3, providing further support for both the effectiveness of our method, and for the potential importance of RNA methylation in cancer. We believe that our methods and results will facilitate the future discovery and validation of many more driver genes from cancer sequencing data.

Results

driverMAPS: a probabilistic model of somatic mutation selection patterns

Our approach is outlined in Figure 1. In brief, we model aggregated exonic somatic mutation counts from many tumor samples (e.g. as obtained from a normal-tumor paired sequencing cohort). Let Y_g denote the mutation count data in gene g . We develop models for Y_g under three different hypotheses: that the gene is a “non- driver gene” (H_0), an “oncogene” (H_{OG}) or a “tumor suppressor gene” (H_{TSG}). Each model has two parts, a background mutation model (BMM), which models the background mutation process, and a selection mutation model (SMM), which models how selection acts on functional mutations. The BMM parameters are shared by all three hypotheses, reflecting the assumption that background mutation processes are the same for cancer driver and non-driver genes. In contrast the SMM parameters are hypothesis-specific, to capture the different selection pressures in oncogenes vs tumor suppressor genes vs non-driver genes. We fit the hypothesis-specific parameters using training sets of known oncogenes¹ (H_{OG}), known TSGs¹ (H_{TSG}), and all other genes (H_0). (This last set will contain some -- as yet unidentified -- driver genes, which will tend to make our methods conservative in terms of identifying new driver genes.) To combine information across tumor types we first

estimate parameters separately in each tumor type, and then stabilize these estimates using Empirical Bayes shrinkage¹⁴.

Having fit these models, we use them to identify genes whose mutation data are most consistent with the driver genes models (H_{OG} and H_{TSG}). Specifically, for each gene g , we measure the overall evidence for g to be a driver gene by the Bayes Factor (likelihood ratio), BF_g , defined as:

$$BF_g := 0.5 [\Pr(Y_g | H_{OG}) + \Pr(Y_g | H_{TSG})] / \Pr(Y_g | H_0).$$

Large values of BF_g indicate strong evidence for g being a driver gene, and at any given threshold we can estimate the Bayesian FDR. For results reported here we chose the threshold by requiring $FDR < 0.1$.

driverMAPS effectively captures factors influencing somatic mutations

We used a total of 734,754 somatic mutations from 20 tumor types in the TCGA project as our input data¹⁵. We focused on single nucleotide somatic variations and extensively filtered input mutation lists to ensure data quality (see Methods). Figure S1 summarizes mutation counts and cohort sizes.

The first step of our method is to estimate parameters of the Background Mutation Model (BMM) using data on synonymous mutations. These parameters capture how mutation rates depend on various “background features” (Table S1), which include mutation type (C>T, A>G, *etc*), CpG dinucleotide context, expression level, replication timing and chromatin conformation (HiC sequencing)⁴. The signs and values of estimated parameters were generally similar across tumor types, and consistent with previous evidence for each feature’s effect on somatic mutation rate. For example, the estimated effect of the feature “expression level” was negative for almost all tumors, consistent with transcriptional coupled repair mechanisms effectively reducing mutation rate (Figure S2).

Our BMM also estimates gene-specific effects, using synonymous mutations of a gene, to allow for variation in somatic mutation rate not captured by any measured feature. Intuitively, the gene-specific effect adjusts a gene’s estimated mutation rate downward if the gene has fewer synonymous mutations than expected based on its known features, and upwards if it has more synonymous mutations than expected. A challenge here is that the small number of mutations per gene (particularly in small genes) could make these estimates inaccurate. Here we address this

using Empirical Bayes methods to improve accuracy, and avoid outlying estimates at short genes that have few potential synonymous mutations (Figure 2a). Effectively, this adjusts a gene's rate only when the gene provides sufficient information to do so reliably (sufficiently many potential synonymous mutations). To demonstrate the reliability of the resulting estimates we use a procedure similar to cross-validation: we estimated each gene's gene-specific effect using its synonymous mutations, and then test the accuracy of the estimate (compared to no gene-specific effect) in predicting the number of nonsynonymous mutations. Figure 2b shows results for SKCM tumors: without gene-specific effect the correlation of observed and expected number of nonsynonymous mutations across genes was 0.56; with gene-specific adjustment the correlation increased to 0.88. Similar improvements were seen for other tumors (Figure S3).

The next step is to estimate parameters of the Selection Mutation Models (SMM), using data on non-synonymous mutations. These parameters capture how the rate of non-synonymous somatic mutations depend on various “functional features” (Table S2-S4), including if loss-of-function (LoF), conservation scores, *etc.* Signs and values of estimated parameters were generally similar across tumor types, and consistent with their expected impact on gene function (Figure 2c). For example, the estimated effect of the “LoF” feature was positive for H_{TSG} and negative for H_{OG} , indicating that loss-of-function mutations are enriched in TSGs and depleted in OGs, as expected from their respective roles in cancer. The intercept terms for both TSG and OG are positive, suggesting that somatic mutations are enriched in both types of cancer driver genes.

The final step is to estimate parameters of the spatial model (HMM, Figure 1), which are designed to capture how somatic mutations may cluster together in “hotspots” in driver genes. Preliminary investigations showed that spatial clustering is generally stronger in known OGs than in known TSGs, and so we fit the spatial model separately for OGs and TSGs in each tumor type (Table S5). Our model identified some tumor types (e.g. BLCA and LUSC, Figure 2d) with strong spatial clustering. In BLCA, the estimated hotspots are very short (mean 1.4bp) and are primarily capturing an excess in recurrent mutations (independent mutations at the same base) compared with expectations (Figure 2d). In LUSC, the clustering extends over slightly longer regions (mean 5.6bp), but still the primary signal is an excess of recurrent mutations (Figure 2d).

driverMAPS improves detection of driver genes

We compared results from driverMAPS with four existing algorithms for predicting driver genes: MutSigCV, OncodriveFML⁹, OncodriveFM¹⁰ and OncodriveCLUST⁸ (see Methods). Besides the full implementation of driverMAPS, we also tried a “basic” version that looks only for an excess of nonsynonymous somatic mutations (without any functional features or spatial model), and a “+feature” version with functional features but not the spatial model. We applied all methods to the same somatic mutation data and compared the genes they identified with a list of “known driver genes” (713 genes) compiled as the union of COSMIC CGC list (version 76)¹⁶, Pan-Cancer project driver gene list² and list from Vogelstein B (2013)¹ (see Supplementary Note). To avoid overfitting of driverMAPS to the training data, we trained driverMAPS with a leave-one-out strategy in these assessments. (It is possible that previously-published methods are biased towards detecting previously-known driver genes; if so then our assessment will artificially favor previously-published methods over driverMAPS).

For each method we computed both the total number of genes detected (at FDR=0.1) (Figure 3a) and the “precision” -- the fraction that are on the list of known driver genes (Figure 3b). All versions of driverMAPS identified more driver genes than either MutSigCV or OncodriveFML, while maintaining a similarly high precision. The full version of driverMAPS (with the spatial and functional features) identified the most genes, and without sacrificing precision. Furthermore, this higher detection rate of driverMAPS was consistent across tumor types (Figure 3c). The other two methods, OncodriveFM and OncodriveCLUST, behaved quite differently, identifying thousands of driver genes but with much lower precision, possibly resulting from poor FDR control. Indeed, the lowest precision was in the tumor types with the highest mutation rates (e.g. BLCA, LUSC, LUAD), suggesting the accuracy of these methods may be affected by mutation rates (Figure S4). While precision of OncodriveFM and OncodriveCLUST showed a negative correlation with mutation rate (Pearson $r = -0.44$ and -0.56), the precision of driverMAPS showed negligible correlation (Pearson $r = 0.05$).

Evaluation of potential novel drivers identified by driverMAPS

Summing across all 20 tumor types, at FDR 0.1, driverMAPS identified 255 known driver genes and 170 putatively novel driver genes (159 unique genes across the 20 tumor types; 70 classified as TSGs and 100 as OGs; Figure 4a, Table S7). Almost half of these putative novel genes were not called by MutSigCV or OncodriveFML. Ten novel genes were found

independently in at least two tumor types (Table 1). This is unlikely to happen by chance (permutation test, $p < 1e^{-4}$), so these genes seem especially good candidates for being genuine driver genes.

Since it is impractical to functionally validate all 170 putative novel genes, we sought other data to support these genes likely being involved in cancer. We first selected three common cancers -- breast, lung and prostate -- and conducted an extensive literature survey for each novel gene identified in these tumor types. Among a total of 22 novel genes, we found clear support in the literature for 20 being involved with cancer biology, either directly implicated as oncogenes or tumor suppressor genes (but not in the list of “known driver genes”) or linked to well-established cancer pathways (Table S8).

We next assessed whether the novel genes were enriched for features often associated with driver genes. Previous studies reported that driver genes tend to be highly expressed⁴ compared with other genes, and indeed we found that, collectively, the novel genes showed significantly higher expression than randomly sampled genes in the corresponding tissues¹⁵ ($p < 1e^{-4}$) (Figure 4b).

Previous studies have also reported that driver genes tend to show enrichment and depletion for different copy-number-variation (CNV) events, depending on their role in cancer. Specifically, OGs are enriched for CNV gains and depleted for CNV loss, whereas TSGs show enrichment for loss and depletion for gains. Consistent with this, we found novel genes identified as OGs are enriched for CNV gain events ($p < 1e^{-4}$) while novel TSGs are depleted ($p = 3e^{-3}$). CNV loss events for novel OGs are depleted compared to novel TSGs and to other genes ($p = 0.04$) (Figure 4c).

We also compared our novel genes with a “cancer dependency map” of 769 genes identified from a large-scale RNAi screening study across 501 human cancer cell lines¹⁷. These are genes whose knockdown affects cell growth differently across cancer cell lines, thus likely representing genes that are critical for tumorigenesis, but not universally essential genes. We found 16 novel driver genes overlapped with this gene list, a significant enrichment compared with random sampling (odds ratio 2.9, $p = 3.7e^{-4}$) (Figure 4d and Table S9).

To test whether our novel genes are functionally related to known cancer driver genes we examined the connectivity of these two sets of genes in the HumanNet¹⁸ gene network, which is built from multiple data sources including protein-protein interactions and gene co-expression.

On average, each novel gene is connected to 3.8 known driver genes, significantly higher than expected by chance ($p = 0.001$). We obtained a similarly significant result using a different gene network, GeneMania¹⁹, which is constructed primarily from co-expression ($p = 0.008$) (Figure 4e).

Finally, we identified enriched functional categories in our novel genes using GO enrichment^{20,21} analysis (by geneSCF²²). Significant GO terms ($FDR < 0.1$, Figure 4f) include many molecular processes directly implicated in cancer, such as transcription initiation and regulation. The significant terms also include several that have not been previously implicated in cancer. Genes NAA25, NAA16 and NAA30 (GO: 0004596) are peptide N-terminal amino acid acetyltransferases²³. NATs are dysregulated in many types of cancer, and knockdown of the NatC complex (NAA12-NAA30) leads to p53-dependent apoptosis in colon and uterine cell lines²⁴. OGDH and OGDHL (GO:0004591) have oxoglutarate dehydrogenase activities and part of the tricarboxylic acid (TCA) cycle²⁵. METTL3 and METTL14 (GO: 0016422) form the heterodimer N6-methyltransferase complex, and are responsible for methylation of mRNA (m⁶A modification)²⁶. This form of RNA modification may influence RNA stability, export and translation, and has been shown to be important for important biological processes such as stem cell differentiation. Our results suggest that this RNA methylation pathway may also play a key role in tumorigenesis, and so we examined the results for these genes in more detail.

METTL3 is a potential TSG in bladder cancer

driverMAPS identified the genes METTL3 and METTL14 as driver genes in the cohorts BLCA (bladder cancer) and UCEC (uterine cancer) respectively. These two genes had relatively low mutation frequencies (4% and 2%) and were not detected by MutSigCV or OncodriveFML. Inspecting the mutations in these two genes, we found many to be “functional” as predicted by annotations, and showed spatial clustering patterns in the MTase domain (Figure 5a). Furthermore METTL3 contained a single synonymous mutation, and METTL14 contained none, suggesting low baseline mutation rates at the two genes. While this manuscript was in preparation, METTL14 was independently identified as a novel TSG in endometrial cancer (Chuan He, unpublished data). We thus focused on METTL3 in bladder cancer.

To gain further insights into the potential impact of the somatic mutations in METTL3, we performed structural analysis. By mapping mutations in the MTase domain of METTL3 to its

crystal structure²⁷, we found them to be concentrated in two regions: one close to the binding site of S-Adenosyl methionine (AdoMet, donor of the methyl group) and the other in the putative RNA binding groove at the interface between METTL3 and METTL14 (Figure 5b). The region close to the AdoMet binding site contains seven mutations: E532K, E532Q, E516K, D515Y, P514T, H512Q and E506K. Position E532 has been reported to form direct water-mediated interactions with AdoMet²⁷. The other mutations map to gate loop 2 (E506K and E516K map to the start and end; the other three mutations are inside the loop) which is known to undergo significant conformational change before and after AdoMet binding. Thus all these mutations are good candidates for affecting adenosine recognition. The second region, in the METTL3-METTL14 interface, contains mutations R471H, R468Q and E454K, and so these mutations are good candidates for disrupting METTL3-METTL14 interaction. In further support of this, the highly recurrent R298P mutation in METTL14 lies in the binding groove of the METTL14 gene.

We performed functional experiments to test whether mutations (n=7) in the first region affect METTL3 function. In an *in vitro* assay, most mutations reduced methyltransferase activity of METTL3 (Figure S5, see methods) and we chose four mutations (at three positions) for further cell line experiments. In two bladder cell lines (“5637” and “T24”), knock down of METTL3 by siRNA significantly reduced m6A methyltransferase activity (Figure 5c for “5637”, Figure S6a for “T24”). When we tried to rescue this phenotype by transfection of METTL3 mutants, all of the mutations, E532K/Q, E516K and P514T failed to restore methyltransferase activity to original levels (Figure 5c, Figure S6a), suggesting that they are loss-of-function mutations.

We next examined whether disruption of METTL3 is associated with tumor progression. Indeed, knockdown of METTL3 significantly increased cell proliferation. Wild type METTL3 successfully restored the cells to their normal growth rate but none of the mutants could (Figure 5d, Figure S6b).

These results show that somatic mutations in METTL3 may promote cancer cell growth by disrupting the RNA methylation process, and invite further characterization of the role of METTL3 and RNA methylation in tumorigenesis by *in vivo* experiments.

Discussion

We have developed an integrated statistical model-based method, driverMAPS, to identify driver genes from patterns of somatic mutation. By applying this method to data from multiple tumor types from TCGA, we detected 159 novel potential driver genes. We experimentally validated the function of mutations in one gene, METTL3. The remaining genes (Table 1, Table S8-9) are enriched for many biological features relevant to cancer, and appear promising candidates for further investigation.

Compared with previous methods for detecting driver genes, a key feature of driverMAPS is that it models mutation rates at the base-pair level. In particular, it models how these mutation rates vary based on both site-level functional annotations (e.g. synonymous/non-synonymous; conservation; loss-of-function status) as well as unmeasured spatial factors. This model-based approach can be thought of as a powerful extension of methods that detect driver genes by testing for an excess of non-synonymous vs synonymous somatic mutations (e.g. Nik-Zainal *et al*²⁸, Martincorena *et al*⁵), similar to the standard dN/dS test in comparative genomics. Indeed, the stripped-down version of driverMAPS that uses no functional annotation or spatial model is conceptually similar to a dN/dS test: it will identify genes as drivers if they show an excess of non-synonymous mutations, treating all non-synonymous mutations equally. The full version of driverMAPS, by incorporating additional functional annotations, allows that some non-synonymous mutations may be more informative than others in identifying driver genes. Furthermore, by estimating parameters in a single integrated model, our approach learns how to weight and combine the many different sources of information. The results in Figure 3 demonstrate the increased power that comes from these extensions.

Our statistical and experimental results for the mRNA methyltransferase METTL3 add to the growing evidence of links between mRNA methylation and cancer. Indeed, a recent study in myeloid leukemia cell lines²⁹, found that depletion of METTL3 also leads to a cancer-related phenotype. And extensive functional studies of METTL14 in uterine cancer (Chuan He, unpublished data) support a role for this gene in cancer etiology. However, intriguingly, our results on METTL3 in bladder cancer, and the METTL14 results in uterine cancer suggest that they act as tumor suppressor genes, whereas the data on METTL3 in myeloid leukemia cell lines are more consistent with an oncogenic role, with depletion inducing cell differentiation and apoptosis²⁹. Further studies in multiple tumor types therefore seem necessary to properly characterize the role of mRNA methylation in cancer.

Although our model incorporates many features not considered by existing methods, it would likely benefit from incorporating still more features. For example, it may be useful to incorporate data on protein structure, which affects the functional importance of amino acid residues. Further, whereas we currently use the same mutation model for all individuals, it could be helpful to incorporate individual-specific effects such as smoking-induced mutational signatures. Finally, it could be useful to extend the model to incorporate information on non-coding variation, which has been shown to be important for many human diseases including cancer. Although identifying functional non-coding variation remains a major general challenge, extending our model to incorporate features from studies of epigenetic factors such as methylation or open chromatin, has the potential to detect novel driver genes affected by non-coding functional somatic mutations.

Acknowledgements

We thank Wei Du for helpful discussion and Megan McNerney for critical comments of the manuscript. We also thank members of Stephens' and He's labs for many feedbacks during the course of this project. This work was supported by National Institutes of Health (NIH) grants MH110531 (to XH) and HG002585 (to MS).

Code availability

driverMAPS software and procedures to reproduce the results reported in the paper can be accessed through the software website: <https://szhao06.bitbucket.io/driverMAPS-documentation/docs/index.html>.

Data availability

The filtered somatic mutation lists from 20 tumor types that used as input files for driverMAPS and other comparator software are available in Zenodo (DOI: 10.5281/zenodo.1209411).³⁰

Methods

Data preparation

We downloaded somatic single-nucleotide mutations identified in whole exome sequencing (WES) studies for 20 tumor types from TCGA GDAC Firehose (<https://gdac.broadinstitute.org/>). We obtained the MAF files using `firehose_get` (version 0.4.6) (<https://confluence.broadinstitute.org/display/GDAC/Download>) and extracted position and nucleotide change information for all single-nucleotide somatic mutations. See Supplementary notes for the 20 tumor types and abbreviations.

We excluded mutations from hypermutated tumors as they likely reflect distinct underlying mutational processes. We also performed extensive filtering to exclude likely false positive mutations. For each tumor type we then generated a mutation count file that contains mutation counts (aggregated across all individuals in the tumor cohort) of all possible mutations at all sufficiently sequenced positions (see Supplementary notes). For a tumor type with 30 million bases sequenced this produces 90 million possible mutations in the mutation count file (since each nucleotide can mutate to 3 other nucleotides). The majority of counts for these possible mutations are 0s.

For each possible mutation, we annotated it with type and gene information, mutational features and functional features. We defined 9 mutation types based on nucleotide change type (such as A>T, G>A, *etc*) and genomic context (such as if inside CpG) (see Supplementary notes for definitions). We categorized mutations as Synonymous (S) or non-synonymous (NS) as described in “parameter estimation” section below. The mutational features we used include gene expression, replication timing and HiC sequencing downloaded from <http://archive.broadinstitute.org/cancer/cga/mutsig>. We selected 5 functional features describing mutation impact. See Supplementary notes for feature details. The features were added to the mutation count file by ANNOVAR³¹.

Model description

We model each tumor type separately, so here we describe the model for a single tumor type. Let Y_{it} denote the number of mutations of type t (defined by base substitution) at sequenced position i , across all samples in a cohort. Let NS denote the set of non-synonymous mutations. That is, NS is the set of pairs (i, t) such that a mutation of type t at sequence position i would be non-synonymous. (We also include synonymous mutation with a high

splicing impact score in NS ; see Supplementary notes.) Similarly, let S denote the remaining (synonymous) (i, t) pairs.

Background Mutation model

For synonymous mutations we assume the following “background mutation model”:

$$Y_{it} | H_m \sim \text{Poisson}(\mu_{it} \lambda_{g(i)}) \left[\text{for } (i, t) \in S \right], \quad (1)$$

where μ_{it} represents a background mutation rate (BMR) for mutation type t at position i , and $\lambda_{g(i)}$ represents a gene-specific effect for the gene $g(i)$ that contains sequence position i . Note that the parameters of this BMM do not depend on the model m , so $P(Y^S | H_m)$ is the same for all m .

We allow the BMRs to depend on mutational features (e.g. the expression level of the gene) using a log-linear model:

$$\log \mu_{it} = \beta_{0t}^b + \sum_j x_{ij}^b \beta_j^b, \quad (2)$$

where x_{ij}^b denotes the j -th background feature of position i (not dependent on mutation type), β_{0t}^b controls the baseline mutation rate of type t , and β_j^b is the coefficient of the j -th feature. The values x_{ij}^b are observed, and the parameters β^b are to be estimated. To indicate the dependence of μ_{it} on parameters β^b we write $\mu_{it}(\beta^b)$.

We assume that the gene-specific effects λ_g have a gamma distribution across genes:

$$\lambda_g \sim \text{Gamma}(\alpha, \alpha), \quad (3)$$

where α is a hyperparameter to be estimated.

Selection Mutation model

For non-synonymous mutations we introduce additional model-specific parameters: γ_{it}^m representing a selection effect (SE) for mutation type t at position i under model m and θ_i^m representing a spatial effect for position i under model m :

$$Y_{it} | H_m \sim \text{Poisson}(\mu_{it} \lambda_{g(i)} \gamma_{it}^m \theta_i^m) \left[\text{for } (i, t) \in NS \right]. \quad (4)$$

For the null model, H_0 , we assume no selection or spatial effect: $\gamma_{it}^0 = \theta_i^0 = 1$.

For other models, $m = OG, TSG$, we allow the selection effect to depend on functional features (e.g. the assessed deleteriousness of the mutation), using a log-linear model:

$$\log \gamma_{it}^m = \beta_0^{f,m} + \sum_j x_{ijt}^f \beta_j^{f,m}, \quad (5)$$

where x_{ijt}^f denotes the j -th functional feature of position i (this depends on mutation type; e.g. at the same position, some mutations may be more deleterious than others), $\beta_j^{f,m}$ is the coefficient of the j -th functional feature and the intercept $\beta_0^{f,m}$ captures the overall change of mutation rate at NS sites regardless of functional impact. To indicate the dependence of γ_{it}^m on parameters $\beta^{f,m}$ we write $\gamma_{it}(\beta^{f,m})$.

To model the spatial effects, we use a Hidden Markov Model (HMM) with parameters Θ^m ,

$$\theta^m \sim f_{\text{HMM}}(\cdot; \Theta^m), \quad (6)$$

In brief, this HMM allows for the presence of mutation “hotspots” -- contiguous base-pairs with a higher rate of mutation -- and the parameters include the average hotspot length and intensity of selection (ρ). See Supplementary note for details.

Parameter estimation

Background mutation model

To simplify inference we took a sequential approach to parameter estimation. First we infer parameters β^b, α of the BMM using the synonymous mutation data at all genes. Let S_g denote the subset of synonymous mutations S in gene g , and $Y_g^{S_g}$ denote the corresponding observed counts:

$$Y_g^{S_g} = \{Y_{it} : (i, t) \in S_g\}. \quad (7)$$

Based on the synonymous mutation data, the likelihood for gene g is:

$$P(Y_g^{S_g} | \beta^b, \alpha) = \int \prod_{i,t \in S_g} P(Y_{it} | \mu_{it}(\beta^b), \lambda_g) p(\lambda_g | \alpha) d\lambda_g, \quad (8)$$

which has a closed form (see Supplementary note). Assuming independence across genes yields the likelihood for synonymous mutations:

$$L^S(\beta^b, \alpha) := \prod_g P(Y^{S_g} | \beta^b, \alpha). \quad (9)$$

We maximize this likelihood, using numerical optimization, to obtain estimates $\widehat{\beta^b}, \hat{\alpha}$ for β^b, α . By ignoring the non-synonymous mutation data when fitting the BMM we may lose some efficiency in principle, but we gain considerable simplification in practice.

Selection mutation model

We next estimate the model-specific parameters $\beta^{f,m}$. For $m = OG, TSG$. During this step we ignore the HMM model (i.e. we set $\theta_i^m = 1$), motivated by the fact that spatially-clustered mutations are relatively rare and so should not significantly impact the estimates of $\beta^{f,m}$.

For $m = OG$ we estimate $\beta^{f,m}$ using the non-synonymous mutation data from a curated list G_{OG} of 53 OGs. Estimation for $\beta^{f,TSG}$ is identical except that we replace this list with a curated list G_{TSG} of 71 TSGs. Let G_m denote these sets of training genes. Let Y^{NS_g} denote the counts of non-synonymous mutations in gene g .

Assuming independence across genes, the likelihood for $\beta^{f,m}$ is:

$$L(\beta^{f,m}) = \prod_{g \in G_m} P(Y^{NS_g}, Y^{S_g} | \beta^{f,m}) \propto \prod_{g \in G_m} P(Y^{NS_g} | \beta^{f,m}, Y^{S_g}) \quad (10)$$

where the second line follows because $P(Y^{S_g} | \beta^{f,m})$ does not depend on $\beta^{f,m}$. The term in this likelihood for gene g is given by:

$$P(Y^{NS_g} | \beta^{f,m}, Y^{S_g}) = \int \prod_{i,t \in NS_g} P(Y_{it} | \mu_{it}(\widehat{\beta^b}), \gamma_{it}(\beta^{f,m}), \lambda_g) P(\lambda_g | Y^{S_g}, \hat{\alpha}) d\lambda_g. \quad (11)$$

It can be shown that

$$\lambda_g | Y^{S_g}, \hat{\alpha} \sim \text{Gamma}(\hat{\alpha} + y_g^S, \hat{\alpha} + \mu_g^S), \quad (12)$$

where μ_g^S and y_g^S are, respectively, the expected (considering only mutational features) and observed number of synonymous mutations in gene g (see Supplementary notes). The conditional mean of this distribution is $\frac{\hat{\alpha} + y_g^S}{\hat{\alpha} + \mu_g^S}$, so if $y_g^S > \mu_g^S$, then $E(\lambda_g | Y^{S_g}, \hat{\alpha}) > 1$.

We obtained the MLE of $\beta^{f,m}$ by maximizing the likelihood (Equation 10) numerically, and obtain corresponding estimated standard errors using the curvature of the likelihood (see Supplementary notes). In tumor types with low mutation rates or sample sizes, these standard

errors can be relatively large, so we borrow information from other tumor types to “stabilize” these estimates. Specifically we use the adaptive shrinkage method¹⁴ to “shrink” estimated values of $\beta^{f,m}$ in each tumor type towards the mean across all tumor types. This shrinkage effect is strongest for tumor types with large standard errors (Figure S7).

HMM parameters

Having estimated β^b, α and $\beta^{f,m}$, we fix their values and estimate the HMM parameters Θ^m for $m = OG, TSG$. The likelihood function involves marginalization of the hidden states of the Markov chain, which can be performed efficiently using standard methods for HMMs. We estimate Θ^m by maximizing this likelihood numerically. See Supplementary note for details.

Gene classification

Having estimated the model parameters as above, for each gene g , we compute its Bayes Factor for being a driver gene as:

$$BF := \frac{0.5P(Y_g^{NS}, Y_g^{S_g} | H_{OG}) + 0.5P(Y_g^{NS}, Y_g^{S_g} | H_{TSG})}{P(Y_g^{NS}, Y_g^{S_g} | H_0)}. \quad (13)$$

The equal weights in the numerator of this BF assume that OGs and TSGs are equally common. This BF simplifies to

$$BF = \frac{0.5P(Y_g^{NS} | Y_g^{S_g}, H_{OG}) + 0.5P(Y_g^{NS} | Y_g^{S_g}, H_{TSG})}{P(Y_g^{NS} | Y_g^{S_g}, H_0)}, \quad (14)$$

because $P(Y_g^{S_g} | H_m)$ is the same for every m . Computing the terms $P(Y_g^{NS} | Y_g^{S_g}, H_m)$ is performed using (Equation 11) above, substituting the estimated model parameters for each model m (see Supplementary notes).

After obtaining the BFs, we can compute the posterior probability of being a driver gene (either *OG* or *TSG*) for every gene, and estimate the Bayesian FDR³² for any given BF threshold. This step requires estimation of the proportion of driver genes, which we do by maximum likelihood (see Supplementary notes).

Comparison of gene prediction results from different methods

When comparing methods, we used the same mutation data (after filtering) and the same nominal FDR threshold (0.1) for each method. Because driverMAPS used 124 known cancer genes as a training set, to avoid bias towards this subset of genes when computing precision or power for driverMAPS, we ran MAPs using a leave-one-out strategy. We perform 124 runs, each

time omitting one TSG/OG from the training set and estimating model parameters from the remaining genes, and then count the omitted gene as “significant” only if this TSG/OG is significant (FDR<0.1) in this run. We then calculate precision as the percentage of significant known cancer genes of all significant genes. All data related to driverMAPS (basic, +feature and full version) presented in Figure 3 were obtained in this way. In fact, estimated model parameters are quite stable across runs, and so the overall result is similar to a single run not using this “leave-one-out” strategy.

Cell lines, siRNA knockdown and plasmid transfection

The T24 cells used in this study were purchased from ATCC (HTB-4) and grown in McCoy’s 5A medium (Gibco, 16600) supplemented with 10% FBS (Gibco), and 1% Penicillin-Streptomycin (Gibco, 15140). The 5637 cells used in this study were purchased from ATCC (HTB-9) and grown in RPMI-1640 medium (Gibco, 11875) supplemented with 10% FBS and 1% Penicillin-Streptomycin. Construction of the pcDNA3 plasmids for the expression of METTL3 in mammalian cells was described previously. All siRNAs were ordered from QIAGEN. Allstars negative control siRNA (1027281) was used as siRNA control. Sequences METTL3 is 5’-CGTCAGTATCTTGGGCAAGTT-3’. Transfection was achieved by using Lipofectamine RNAiMAX (Invitrogen) for siRNA, or Lipofectamine 2000 (Invitrogen) for the plasmids following manufacturer’s protocols.

***In vitro* assay for m⁶A methyltransferase activity**

The recombinant, His-tagged proteins METTL14 with wildtype or mutant METTL3 were expressed in 1 LB Ecoli expression system and purified through Ni-NTA affinity column according to a previously published procedure³³. Protein purity was assessed by SDS-PAGE, and protein concentration was determined by UV absorbance at 280 nm. We performed an *in vitro* methyltransferase activity assay in a 50 μ L reaction mixture containing the following components: 0.15 nmol RNA probe, 0.15 nmol each fresh recombinant protein (METTL14 combination with an equimolar ratio of METTL3 or mutant METTL3), 0.8 mM d3-SAM, 80 mM KCl, 1.5 mM MgCl₂, 0.2 U μ L⁻¹ RNasin, 10 mM DTT, 4% glycerol and 15 mM HEPES (pH 7.9). The reaction was incubated for 12 h at 16 °C, RNA was recovered by phenol/chloroform (low pH) extraction followed by ethanol precipitation and was digested by

nuclease P1 and alkaline phosphatase for LC-MS/MS detection. The nucleosides were quantified by using the nucleoside-to-base ion mass transitions of 285 to 153 (*d3*-m⁶A) and 284 to 152 (G).

RNA isolation

Total RNA was isolated with TRIZOL reagent (Invitrogen). mRNA was extracted from the total RNA using the Dynabeads[®] mRNA Purification Kit (Invitrogen), followed by removal of contaminating rRNA with the RiboMinus transcriptome isolation kit (Invitrogen). mRNA concentration was measured by UV absorbance at 260 nm.

LC-MS/MS quantification of m⁶A in poly(A)-mRNA

100-200 ng of mRNA was digested by nuclease P1 (2 U) in 25 μ L of buffer containing 25 mM of NaCl, and 2.5 mM of ZnCl₂ at 42 °C for 2 h, followed by the addition of NH₄HCO₃ (1 M, 3 μ L) and alkaline phosphatase (0.5 U) and incubation at 37 °C for 2 h. The sample was then filtered (0.22 μ m pore size, 4 mm diameter, Millipore), and 5 μ L of the solution was injected into the LC-MS/MS. The nucleosides were separated by reverse phase ultra-performance liquid chromatography on a C18 column with online mass spectrometry detection using Agilent 6410 QQQ triple-quadrupole LC mass spectrometer in positive electrospray ionization mode. The nucleosides were quantified by using the nucleoside to base ion mass transitions of 282 to 150 (m⁶A), and 268 to 136 (A). Quantification was performed by comparison with a standard curve obtained from pure nucleoside standards run with the same batch of samples. The ratio of m⁶A to A was calculated based on the calibrated concentrations.

Cell proliferation assay.

5000 cells were seeded per well in a 96-well plate. The cell proliferation was assessed by assaying the cells at various time points using the CellTiter 96[®] Aqueous One Solution Cell Proliferation Assay (Promega) following the manufacturer's protocols. For each cell line tested, the signal from the MTS assay was normalized to the value observed ~24 hours after seeding.

References

1. Vogelstein, B. *et al.* Cancer Genome Landscapes. *Science* (80-.). **339**, 1546 LP-1558 (2013).
2. Network, T. C. G. A. R. *et al.* The Cancer Genome Atlas Pan-Cancer analysis project. *Nat Genet* **45**, 1113–1120 (2013).
3. Lawrence, M. S. *et al.* Discovery and saturation analysis of cancer genes across 21 tumour types. *Nature* **505**, 495–501 (2014).
4. Lawrence, M. S. *et al.* Mutational heterogeneity in cancer and the search for new cancer-

- associated genes. *Nature* **499**, 214–8 (2013).
5. Martincorena, I. *et al.* Universal Patterns of Selection in Cancer and Somatic Tissues. *Cell* **171**, 1029–1041.e21 (2017).
6. Dees, N. D. *et al.* MuSiC: Identifying mutational significance in cancer genomes. *Genome Res.* **22**, 1589–1598 (2012).
7. Korthauer, K. D. & Kendziorski, C. MADGiC: a model-based approach for identifying driver genes in cancer. *Bioinformatics* **31**, 1526–1535 (2015).
8. Tamborero, D., Gonzalez-Perez, A. & Lopez-Bigas, N. OncodriveCLUST: exploiting the positional clustering of somatic mutations to identify cancer genes. *Bioinformatics* **29**, 2238–2244 (2013).
9. Mularoni, L., Sabarinathan, R., Deu-Pons, J., Gonzalez-Perez, A. & López-Bigas, N. OncodriveFML: a general framework to identify coding and non-coding regions with cancer driver mutations. *Genome Biol.* **17**, 128 (2016).
10. Gonzalez-Perez, A. & Lopez-Bigas, N. Functional impact bias reveals cancer drivers. *Nucleic Acids Res.* **40**, (2012).
11. Davoli, T. *et al.* Cumulative Haploinsufficiency and Triplosensitivity Drive Aneuploidy Patterns and Shape the Cancer Genome. *Cell* **155**, 948–962 (2013).
12. Ng, P. C. & Henikoff, S. SIFT: predicting amino acid changes that affect protein function. *Nucleic Acids Res.* **31**, 3812–3814 (2003).
13. Adzhubei, I. *a et al.* A method and server for predicting damaging missense mutations. *Nat. Methods* **7**, 248–9 (2010).
14. Stephens, M. False discovery rates: a new deal. *Biostatistics* **18**, 275–294 (2017).
15. Broad Institute TCGA Genome Data Analysis Center. *Analysis-ready standardized TCGA data from Broad GDAC Firehose stddata__2015_06_01 run.* Broad Institute of MIT and Harvard (2016). doi:10.7908/C1251HBG
16. Forbes, S. A. *et al.* COSMIC: somatic cancer genetics at high-resolution. *Nucleic Acids Res.* **45**, D777–D783 (2017).
17. Tsherniak, A. *et al.* Defining a Cancer Dependency Map. *Cell* **170**, 564–576.e16 (2017).
18. Lee, I., Blom, U. M., Wang, P. I., Shim, J. E. & Marcotte, E. M. Prioritizing candidate disease genes by network-based boosting of genome-wide association data. *Genome Res.* **21**, 1109–1121 (2011).
19. Warde-Farley, D. *et al.* The GeneMANIA prediction server: biological network integration for gene prioritization and predicting gene function. *Nucleic Acids Res.* **38**, W214–W220 (2010).
20. Ashburner, M. *et al.* Gene Ontology: tool for the unification of biology. *Nat. Genet.* **25**, 25 (2000).
21. Consortium, G. O. Expansion of the Gene Ontology knowledgebase and resources. *Nucleic Acids Res.* **45**, D331–D338 (2016).
22. Subhash, S. & Kanduri, C. GeneSCF: a real-time based functional enrichment tool with support for multiple organisms. *BMC Bioinformatics* **17**, 365 (2016).
23. Polevoda, B., Arnesen, T. & Sherman, F. A synopsis of eukaryotic N α -terminal acetyltransferases: nomenclature, subunits and substrates. in *BMC proceedings* **3**, S2 (BioMed Central, 2009).
24. Mughal, A. A. *et al.* Knockdown of NAT12/NAA30 reduces tumorigenic features of glioblastoma-initiating cells. *Mol. Cancer* **14**, 160 (2015).
25. Bunik, V. I. & Degtyarev, D. Structure–function relationships in the 2-oxo acid

- dehydrogenase family: Substrate-specific signatures and functional predictions for the 2-oxoglutarate dehydrogenase-like proteins. *Proteins Struct. Funct. Bioinforma.* **71**, 874–890 (2008).
26. Roundtree, I. A., Evans, M. E., Pan, T. & He, C. Dynamic RNA modifications in gene expression regulation. *Cell* **169**, 1187–1200 (2017).
 27. Wang, X. *et al.* Structural basis of N6-adenosine methylation by the METTL3–METTL14 complex. *Nature* **534**, 575 (2016).
 28. Nik-Zainal, S. *et al.* Landscape of somatic mutations in 560 breast cancer whole-genome sequences. *Nature* **534**, 47 (2016).
 29. Vu, L. P. *et al.* The N 6-methyladenosine (m 6 A)-forming enzyme METTL3 controls myeloid differentiation of normal hematopoietic and leukemia cells. *Nat. Med.* **23**, 1369 (2017).
 30. Zhao, S. TCGA filtered dataset used in driverMAPS paper. (2018). doi:10.5281/ZENODO.1209412
 31. Wang, K., Li, M. & Hakonarson, H. ANNOVAR: functional annotation of genetic variants from high-throughput sequencing data. *Nucleic Acids Res.* **38**, e164–e164 (2010).
 32. Newton, M. A., Noueiry, A., Sarkar, D. & Ahlquist, P. Detecting differential gene expression with a semiparametric hierarchical mixture method. *Biostatistics* **5**, 155–176 (2004).
 33. Wang, P., Doxtader, K. A. & Nam, Y. Structural basis for cooperative function of Mettl3 and Mettl14 methyltransferases. *Mol. Cell* **63**, 306–317 (2016).
 34. Pollard, K. S., Hubisz, M. J., Rosenbloom, K. R. & Siepel, A. Detection of nonneutral substitution rates on mammalian phylogenies. *Genome Res.* **20**, 110–121 (2010).
 35. Reva, B., Antipin, Y. & Sander, C. Predicting the functional impact of protein mutations: application to cancer genomics. *Nucleic Acids Res.* **39**, e118–e118 (2011).
 36. Von Mering, C. *et al.* STRING: known and predicted protein–protein associations, integrated and transferred across organisms. *Nucleic Acids Res.* **33**, D433–D437 (2005).

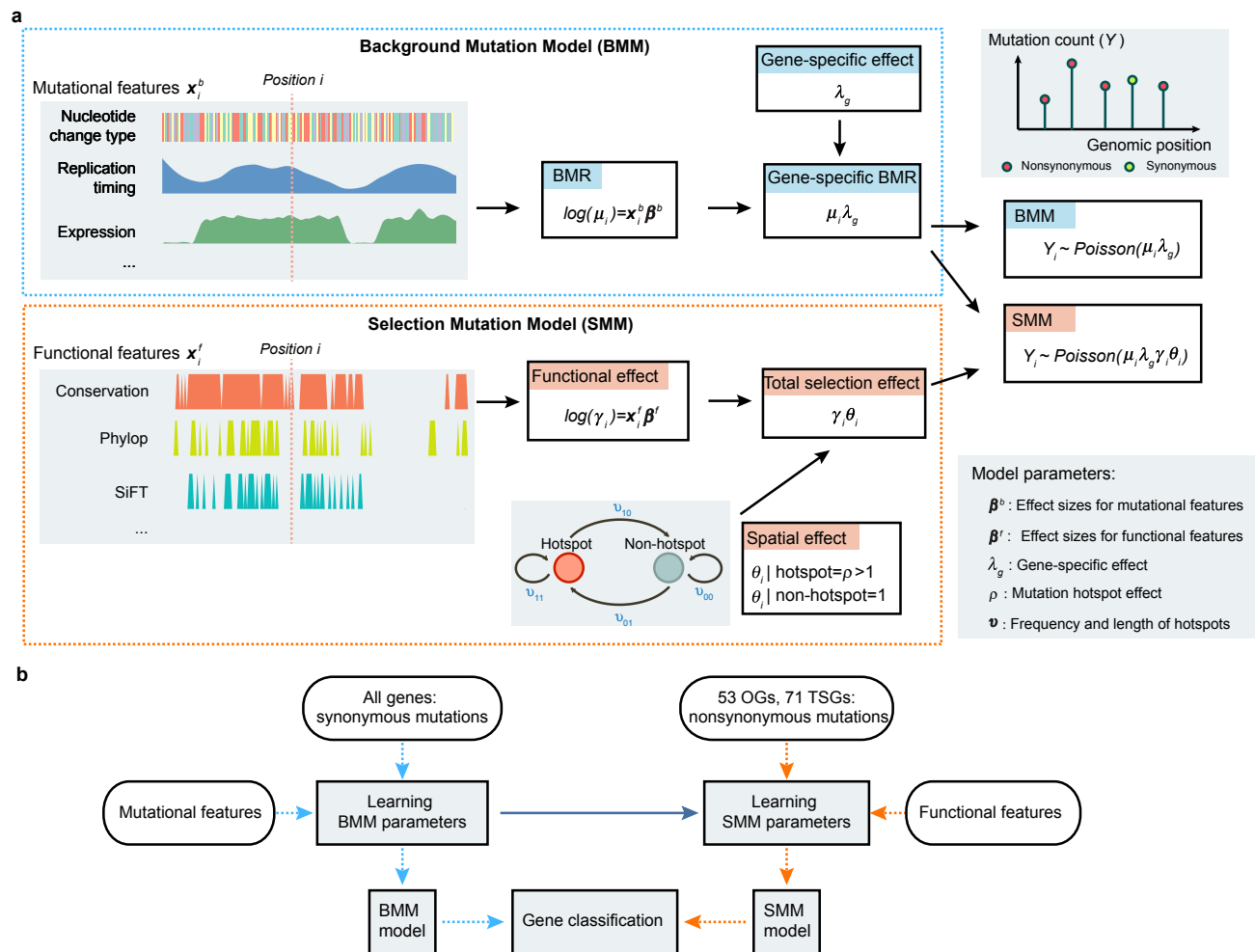


Figure 1 Overview of the model-based framework driverMAPS for cancer driver gene discovery

(a) Base-level Bayesian statistical modeling of mutation count data in driverMAPS. For positions without selection, the observed mutation rate is modeled by Background Mutation Model (BMM). Under BMM, the Background Mutation Rate (BMR)(μ_i) is determined by the log-linear model that takes into account known mutational features and further adjusted by gene-specific effect (λ_g) to get gene-specific BMR ($\mu_i \lambda_g$). For positions under selection, the observed mutation rate is modeled as gene-specific BMR adjusted by selection effect (Selection Mutation Model, SMM). The selection effect has two components: functional effect (γ_i) takes into account functional features of the position by the log-linear model and spatial effect (θ_i) takes into account the spatial pattern of mutations by Hidden Markov Model. For both BMM and SMM, given the mutation rate, the observed mutation count data is modeled by Poisson distribution. Note: we simplify the model to only show mutation rate at position i , ignoring allele specific effect for illustration purposes. See Methods for full parameterization. **(b)** Gene classification workflow. Parameters in BMM are estimated using synonymous mutations from all genes. This set of parameters is fixed when inferring parameters in SMM. To infer parameters in SMM, we use nonsynonymous mutations from known OGs or TSGs. driverMAPS then performs model selection by computing gene-level Bayes Factors to prioritize cancer genes.

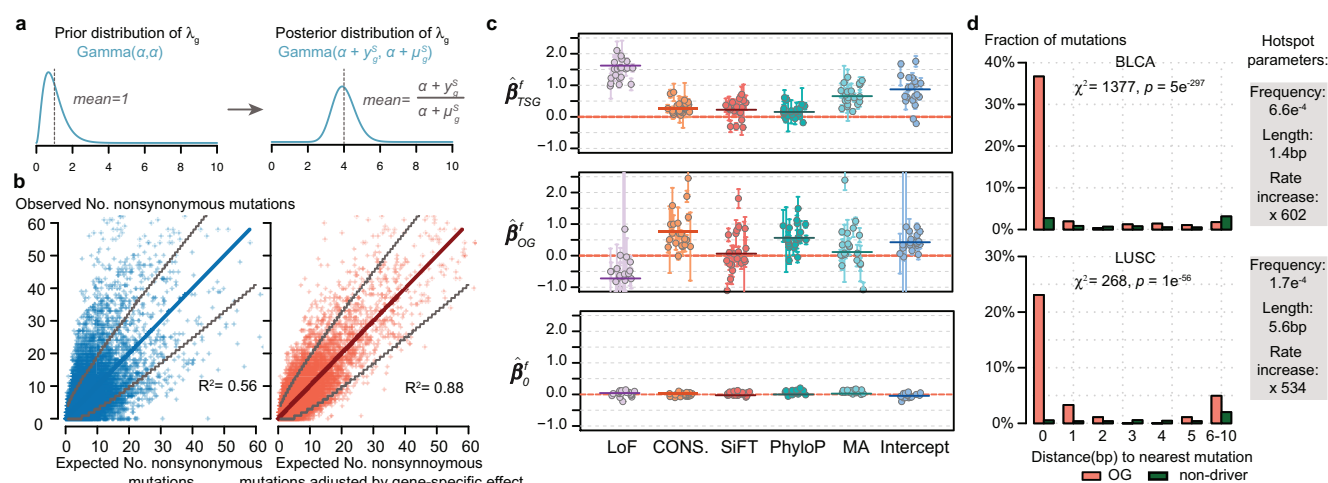


Figure 2 Parameter estimation results for gene-specific, functional and spatial effects

(a) Schematic representation of how fitting synonymous mutation data affects estimation of gene-specific effect (λ_g). Note the difference between the prior and posterior distributions of λ_g . α is a hyperparameter, y_g^S and μ_g^S are the observed and expected number of synonymous mutations in gene g , respectively. **(b)** Improved fitting of observed number of nonsynonymous mutations in genes with gene-specific effect adjustment. Data from tumor type SKCM was used. The adjustment here is the posterior mean of λ_n fitting synonymous mutation data ($\frac{\alpha + y_g^S}{\alpha + \mu_g^S}$). Each dot represents one gene. Grey lines indicate upper and lower bounds of 99% confidence interval from Poisson test. The diagonal line has slope =1 and R^2 was calculated using this as the regression line. **(c)** Effect sizes for five functional features and average increased mutation rate for TSGs (top), OGs (middle) and non-driver genes (bottom). Each dot represents an estimate from one tumor type. Horizontal bars represent mean values after shrinkage. All features are binarily coded. LoF, loss-of-function (nonsense or splice site) mutations or not. CONS., amino acid conservation; SiFT, PhyloP and MA, predictions from software SiFT¹², PhyloP³⁴ and MutationAssessor³⁵, respectively; intercept, average increased mutation rate. **(d)** Fraction of mutations that has the nearest mutation 0,1,2,... bp away, where 0bp means recurrent mutations. Data from tumor type BLCA and LUSC was used. The test statistics χ^2 and p values were obtained in the spatial model selection procedure (see method, Table S6). Inferred parameters related to the spatial model are shown on the right.

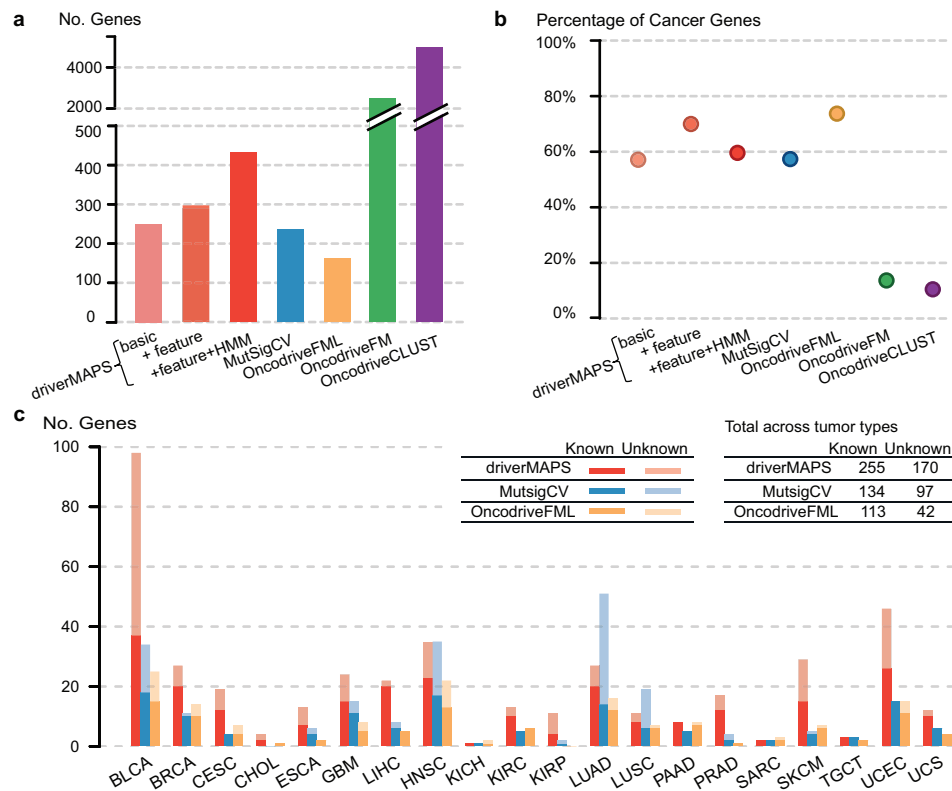


Figure 3 driverMAPS predicts cancer genes with high accuracy and increased power

(a) Total number of predicted driver genes aggregating across all cancer types. driverMAPS (Basic), driverMAPS with no functional features information and no modeling of spatial pattern; driverMAPS (+feature), driverMAPS with all five functional features in Figure 2, no modeling of spatial pattern; driverMAPS (+feature + HMM), complete version of driverMAPS with all five functional features and spatial pattern. **(b)** Percentage of known cancer genes among predicted driver genes aggregating across all cancer types. **(c)** Number of significant genes at FDR=0.1 stratified by tumor type. For all “Unknown” genes included here, we verified mutations by visual inspection of aligned reads using files from Genomic Data Commons (see Supplementary notes). Total numbers of known and unknown significant genes aggregating across all cancer types are summarized in the table on the topright side.

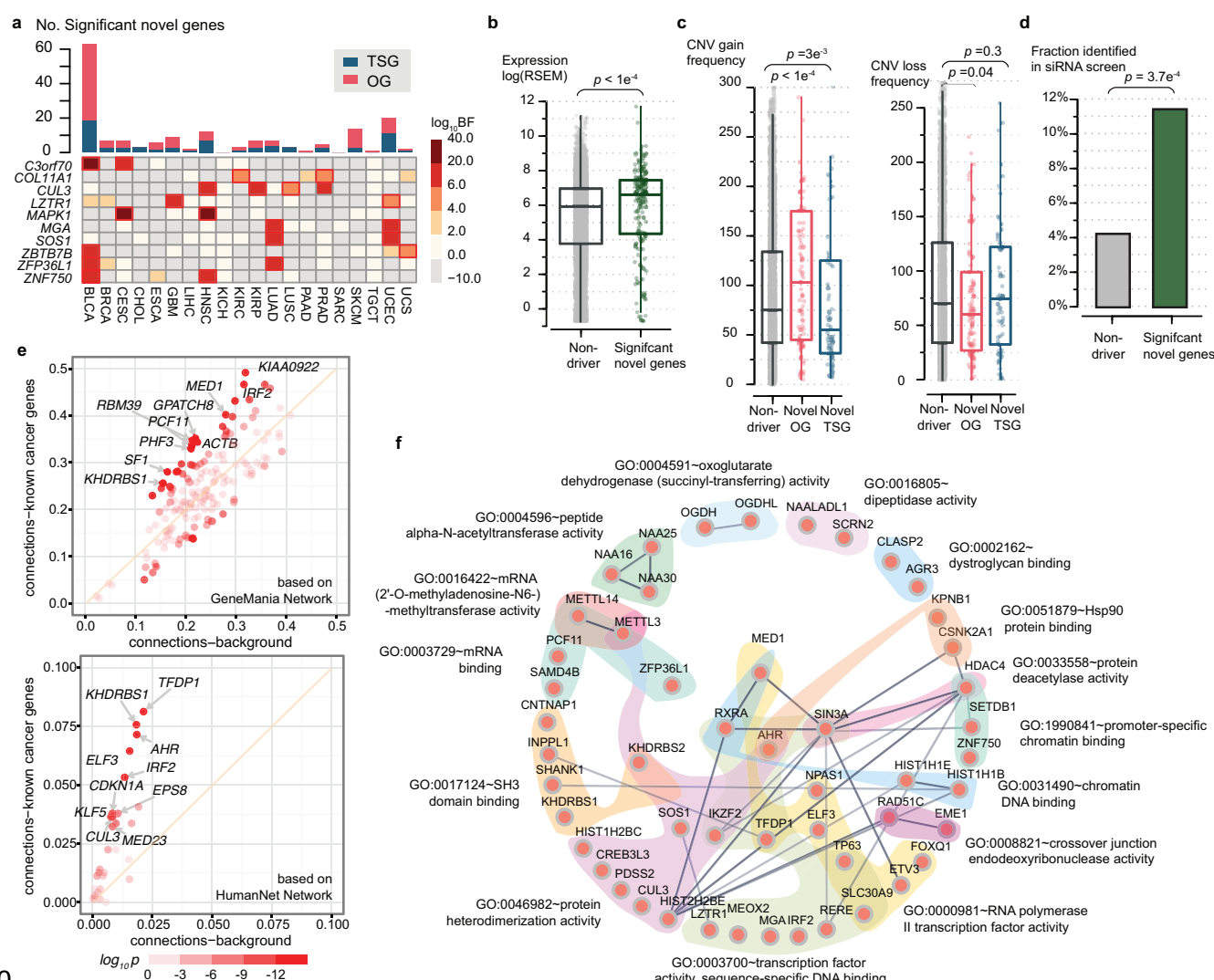


Figure 4 Evaluation of novel cancer genes predicted by driverMAPS

(a) Overview of predicted novel cancer genes. Top, number of novel genes in each cancer type. Bottom, heatmap of Bayes factors (BF) for recurrent novel genes across tumor types. Significant Bayes factors are highlighted by red boxes. **(b-d)** Predicted novel cancer genes show known cancer gene features. For each feature, quantification of the feature level in the novel cancer gene set was compared to the non-driver (neither known or predicted) gene set. The features are gene expression levels¹⁵ stratified by tumor types the novel genes were identified from **(b)**, similarly stratified copy number gain/loss frequencies¹⁵ **(c)** and fraction of genes identified in a siRNA screen study¹⁷ **(d)**. In **(b)** and **(c)**, the center line, median; box limits, upper and lower quartiles. **(e)** Enriched connectivity of a predicted gene with 713 known cancer genes (Y-axis) compared to with all genes ($n=19,512$, X-axis). Connectivity of a selected gene with a gene set is defined as the number of connections between the gene and gene set found in a network database divided by the size of the gene set. Each dot represents one of the 159 novel genes with 10 most enriched ones labeled. Color of dots indicates two-sided Fisher exact p value for enrichment. **(f)** Significantly enriched GO-term gene sets ($FDR < 0.1$, "molecular function" domain) in predicted novel cancer genes. GO-term^{20,21} gene sets are indicated by distinct background colors. Links among genes represent interaction based on STRING network database³⁶ with darker color indicating stronger evidence.

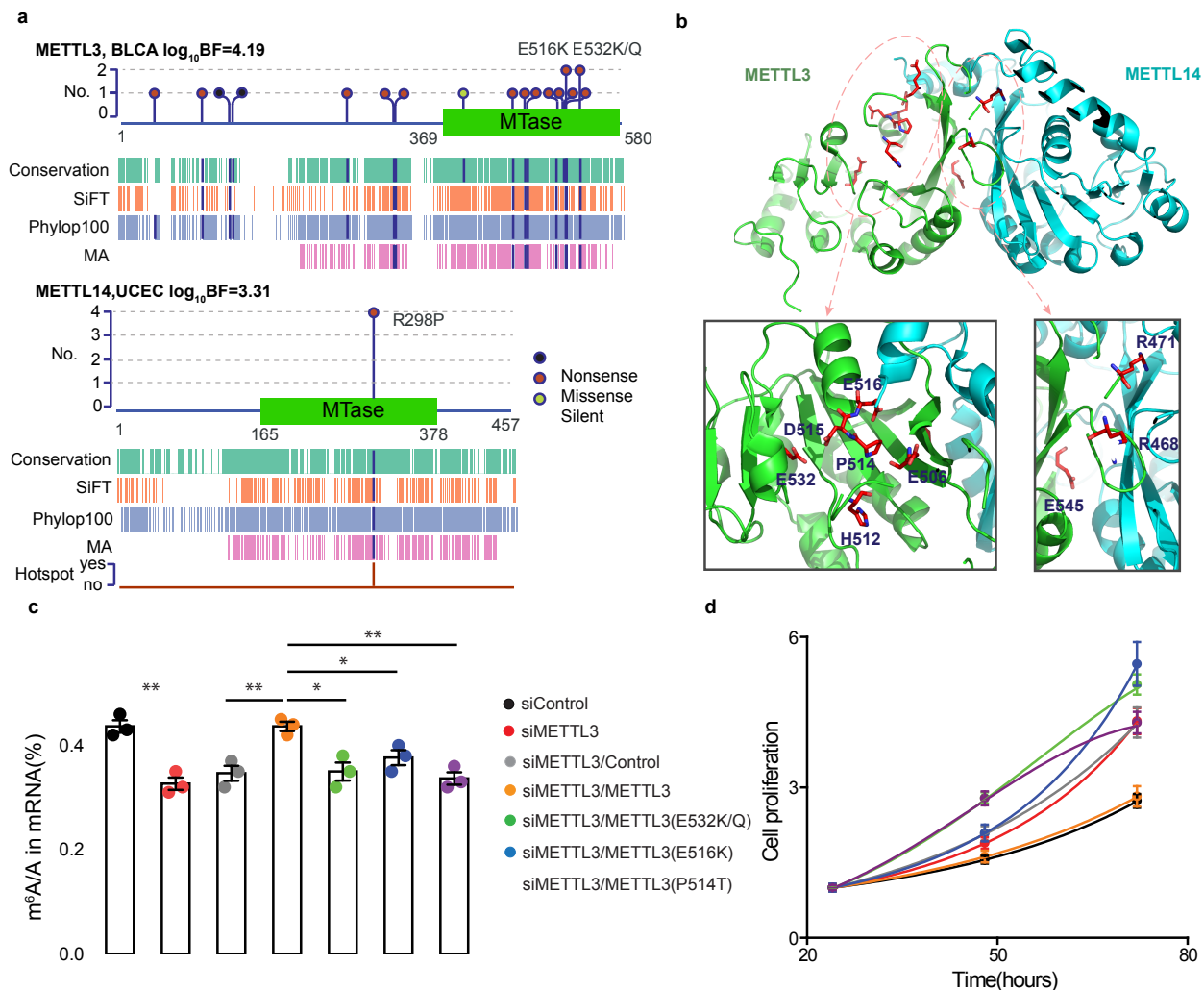


Figure 5 Functional validation of METTL3 as a TSG in bladder cancer

(a) Features of mutations in METTL3 and its heterodimerization partner METTL14. We show schematic representations of protein domain information and mark mutation positions by “lollipops”. Recurrent mutations are labeled above. Start and end of domain residues are labeled below. Dark blue bars in aligned annotation tracks indicate the mutation is predicted as “functional”. Track “Hotspot” is the indicator of whether the mutation is in hotspot or not in driverMAPS’s spatial effect model (See supplementary note). **(b)** Structural context of METTL3 mutations revealed two regional clusters. Top, structure of METTL3 (residues 369–570) and METTL14 (residues 117–402) complex (PDB ID: 5IL0) with mutated residues in stick presentation. Bottom, zoom-in views of the two regions with mutated residues labeled. **(c)** Impaired m⁶A RNA methyltransferase activity of mutant METTL3 in bladder cancer cell line “5637”. LC-MS/MS quantification of the m⁶A/A ratio in polyA-RNA in METTL3 or Control knockdown cells, rescued by overexpression of wildtype or mutant METTL3 is shown. **(d)** Mutant METTL3 decreased proliferation of “5637” cells. Proliferation of METTL3 or Control knockdown cells, rescued by overexpression of wildtype or mutant METTL3 in MTS assays is shown. Cell proliferation is calculated as the MTS signal at the tested time point normalized to the MTS signal ~ 24 hours after cell seeding. For all experiments in **(c-d)**, number of biological replicates is 3 and error bars indicate mean ± s.e.m. *, $p < 0.05$; **, $p < 0.01$ by two sided t -test. Legend is shared between **(c)** and **(d)**.

88

89 **Table 1 Novel significant drivers found in at least two tissue types**

Gene	#Missense	#LoF	#Silent	log ₁₀ BF	Tumor	Function
C3orf70	14/3	1/1	0/0	9.3/3.8	BLCA/CESC	Unknown
COL11A1	7/13	4/2	0/0	2.2/2.2	KIRC/PRAD	Collagen formation, expression associated with colorectal, ovarian cancers, etc (23934190, 11375892)
CUL3	15/8/4	5/4/0	1/0/0	3.5/3.8/2.6	HNSC/KIRP/PRAD	Core component of E3 ubiquitin ligase complex, with many downstream targets affecting carcinogenesis, like NRF2 (24142871)
LZTR1	9/10	0/1	0/2	2.9/2.1	GBM/UCEC	Adaptor of CUL3-containing E3 ligase complexes, inactivation drives glioma self renewal and growth (23917401)
MAPK1	9/7	0/1	0/0	15.1/12.8	CESC/HNSC	MAP kinase. The MAPK/ERK cascade has important well characterized and important roles in cancer (17496922)
MGA	35/11	16/5	5/3	3.8/2.7	LUAD/UCEC	Dual-specificity transcription factor, can inhibit MYC-dependent cell transformation (10601024)
SOS1	12/7	1/0	3/0	3.5/7.0	LUAD/UCEC	Guanine nucleotide exchange factor for RAS proteins, which are well-known for roles in cell proliferation (17486115)
ZBTB7B	11/5	1/1	0/0	6.2/2.3	BLCA/UCS	Transcriptional regulator of lineage commitment of immature T-cell precursors (17878336)
ZFP36L1	12/11	4/3	1/0	3.4/5.2	BLCA/LUAD	Involved in mRNA degradation. Deletion leads to T lymphoblastic leukemia (20622884)
ZNF750	17/13	3/7	2/1	3.4/5.1	BLCA/HNSC	An essential regulator of epidermal differentiation. Depletion promotes cell proliferation in ESCA (24686850)

90 We use “/” to separate data obtained from different tumor types as indicated in the “Tumor” column.

91 A brief description of the gene’s function and its known role in cancer is provided in the “Function”
 92 column. Reference PMIDs are given in parentheses.

93